JOURNAL OF GEOPHYSICAL RESEARCH, VOL. 114, A03214, doi:10.1029/2008JA013630, 2009

Auroral arc and oval electrodynamics in the Harang region

O. Marghitu,[1,2] T. Karlsson,[3] B. Klecker,[2] G. Haerendel,[2] and J. McFadden[4]

Received 21 July 2008; revised 19 December 2008; accepted 8 January 2009; published 26 March 2009.

[1] Auroral arcs are typically described in terms of an upward field-aligned current (FAC) sheet above the arc, connected by ionospheric Pedersen current to a downward FAC sheet near the arc. On the basis of data measured by the FAST spacecraft, conjugate with ground optical observations, we present first a wide and stable winter evening arc, where this standard model does not apply. The arc is observed in the Harang region during the growth phase of a modest substorm, poleward of the convection reversal (CR) boundary. Although the magnetic field data suggest the typical configuration, the two FAC sheets appear to be decoupled near the satellite footprint: the upward FAC is fed by the westward electrojet (WEJ), while the downward FAC feeds the eastward electrojet (EEJ). The examination of the arc by the newly developed ALADYN technique confirms this peculiar current topology. For comparison, we apply ALADYN also to a second evening arc, located within the Harang region equatorward from the CR. The arc is confirmed to have the standard configuration, consistent with a former study, but substantial FAC-EJ coupling is inferred in the auroral oval both poleward and equatorward of the arc. A key element for the topology of the current closure is the westward component of the electric field, which influences the relative location of the CR with respect to the large-scale FAC reversal (FR) boundary. As proved by tests on synthetic data, a westward component of the electric field pushes the CR toward the FR, preventing thus the standard FAC closure, while the conductance and FAC pattern shape the CR profile. Since a westward electric field is often measured in the Harang region, the FAC-EJ coupling is expected to be an essential ingredient there. This has important implications for the current closure in the equatorial magnetosphere and for the auroral current circuit in the WEJ region, closely related to the substorm process.

Citation: Marghitu, O., T. Karlsson, B. Klecker, G. Haerendel, and J. McFadden (2009), Auroral arc and oval electrodynamics in the Harang region, *J. Geophys. Res.*, *114*, A03214, doi:10.1029/2008JA013630.

1. Introduction

[2] The traditional view on the current system associated with a stable auroral arc originates with *Boström* [1964]. According to it, an upward field-aligned current (FAC) sheet above the arc connects to a downward FAC sheet nearby through an ionospheric Pedersen current. Because of the increased conductance, a partial Cowling channel, that carries a divergence free Hall electrojet, develops along the arc. In-situ measurements [e.g., *Sugiura*, 1984] provided experimental evidence in support of this configuration, labeled by Boström as ''Type 2''. *Boström* [1964] also suggested an alternative, ''Type 1'' configuration, with filamentary FACs at the end points of the arc continued in the ionosphere by a Pedersen electrojet along the arc. Later on, this configuration was associated with the substorm current wedge and the large-scale convection electrojets [e.g., *Baumjohann*, 1983]. The two models of *Boström* [1964] are reproduced here in Figure 1.

[3] In this paper we analyze the ionospheric current closure for two arc events, on both arc and oval scale, and find that large portions of the electrojets are not divergence free. Although there are significant differences between the two events, in both cases the large-scale Region 1/Region 2 (R1/R2) currents are essentially balanced, and the magnetic field data are consistent with the standard, meridional FAC closure. However, a careful investigation reveals that a substantial fraction of the FAC current closes in the longitudinal direction, by coupling with the eastward electrojet (EEJ) equatorward of the convection reversal (CR) boundary, and with the westward electrojet (WEJ) poleward of the CR.

[4] The overlap of the EEJ at lower latitudes with the WEJ at higher latitudes is a typical Harang region configuration, often realized not only in the premidnight sector but also deep in the evening sector [e.g., *Kauristie et al.*, 2001]. Note that we shall prefer the concept of ''Harang region'' (HR), instead of the more common ''Harang discontinuity'' (HD). According to *Gjerloev and Hoffman* [2001], the HR separates regions of clearly poleward and equatorward

[1]Space Plasma and Magnetometry Group, Institute for Space Sciences, Bucharest, Romania.
[2]Max Planck Institute for Extraterrestrial Physics, Garching, Germany.
[3]Space and Plasma Physics, School of Electrical Engineering, Royal Institute of Technology, Stockholm, Sweden.
[4]Space Sciences Laboratory, University of California, Berkeley, California, USA.

0148-0227/09/2008JA013630$09.00

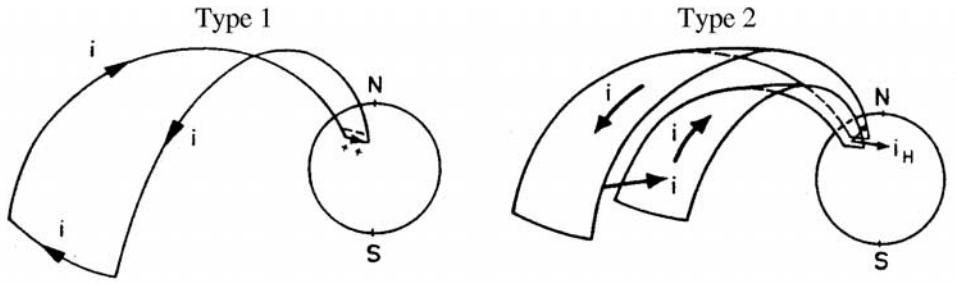

Figure 1. Two configurations of the auroral current circuit predicted by *Boström* [1964].

meridional electric field, and the concept is particularly useful when the electric field at the CR displays "multiple zero crossings or wide regions of very weak electric fields". In the following we shall adopt a slightly different definition, namely we shall understand by "Harang region" that part of the auroral oval where the EEJ at lower latitudes coexists with the WEJ at higher latitudes.

[5] Another typical feature of the Harang region is the westward component of the electric field. From an essentially poleward orientation in the evening sector, the electric field rotates counterclockwise in the Harang region, and reaches an equatorward orientation in the morning sector [e.g., *Baumjohann*, 1983]. A purely meridional electric field is consistent with a CR location at the poleward boundary of the FAC region, and with the standard FAC closure, achieved by meridional Pedersen current. On the other hand, a westward component of the electric field drives a meridional Hall current, that changes the local current closure and, implicitly, the distribution of the meridional electric field across the FAC region. The reconfiguration of the meridional electric field depends on the detailed conductance and FAC profile, but the general result is that the standard FAC closure is prevented over some fraction of the auroral oval.

[6] The auroral arcs in the HR [e.g., *Nielsen and Greenwald*, 1979] are thought to be closely associated with the substorm onset and the formation of the substorm current wedge [e.g., *Koskinen and Pulkkinen*, 1995; *Lyons et al.*, 2003], although recent results by *Weygand et al.* [2008] suggest that this association is more complex than initially believed. A fair representation of the ionospheric electrodynamics in the HR can contribute to a better understanding of the magnetospheric end of the current circuit [e.g., *Akasofu and Kamide*, 1998] and of the substorm overall.

[7] After an introduction of the ALADYN method in section 2, we present and discuss the two events in section 3. Simple tests with synthetic data emphasize the role of the westward electric field in section 4. The limitations of the ALADYN method, the respective contributions of the Hall and Pedersen current to the FAC-EJ coupling, and several implications for the auroral current circuit are discussed in section 5. The paper concludes in section 6 with a summary and prospects for future work.

2. ALADYN Method

[8] The ALADYN method enables a realistic description of the arc electrodynamics [*Marghitu*, 2003; *Marghitu et al.*, 2004]. Provided that the ionospheric conductance is known reasonably well, the method can be extended to larger scales, and used to investigate the auroral electrodynamics across significant fractions of the oval. ALADYN is based on a parametric model, and the parameters are derived by numerical fit to the experimental data. In order to obtain consistent results one can include in the model the ionospheric polarization, a constant longitudinal electric field (providing Hall contribution to the meridional FAC closure), and a divergent electrojet. Here we give a brief account of the ALADYN method, which is detailed in *Marghitu et al.* [2004].

[9] The reference systems used by ALADYN are sketched in Figure 2. The satellite associated system (SAS) has the x axis along the ionospheric footprint of the satellite path, while the arc associated system (AAS) has the ξ axis normal to the arc. The y and η axes complete the respective right-handed systems, with z normal to the plane of Figure 2 and assumed parallel to the magnetic field. The rotation angle θ between the SAS and AAS is derived by minimum variance analysis from the magnetic field data.

[10] The SAS coordinates are appropriate for the input data, while the arc (and oval) symmetry is best expressed in the AAS system. We assume that longitudinal homogeneity, $\partial/\partial\eta = 0$, provides a good approximation for most quantities, with the important exception of the longitudinal current, J_η, allowed to have a constant variation in the longitudinal direction, $\partial J_\eta/\partial\eta = c_1$ (as discussed later in the paper, this variation appears to be caused rather by changes in the conductance than in the electric field). The integration of

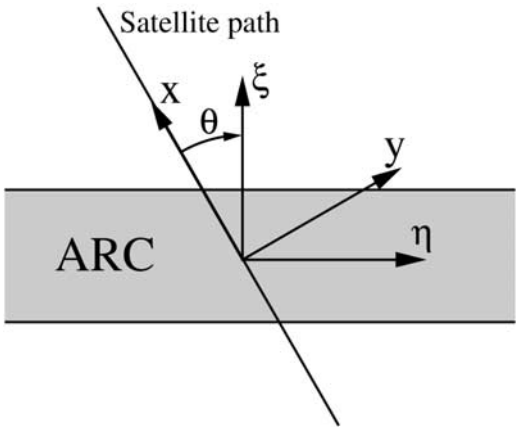

Figure 2. Satellite associated system (x, y) and arc associated system (ξ, η) used by ALADYN.

the current continuity equation, $\nabla \cdot j = 0$, over the height of the ionosphere, yields

$$j_{\parallel} - \frac{\partial J_{\xi}}{\partial \xi} = \frac{\partial J_{\eta}}{\partial \eta} = c_1 \tag{1}$$

In the standard configuration c_1 vanishes and $j_{\parallel}$ closes only at the expense of the variation in J_{ξ}. By allowing for the divergence of J_{η}, a 3D examination of the local current closure becomes possible. The main result to be obtained is that the FAC-EJ coupling can occasionally be dominant, $j_{\parallel} \simeq c_1$.

[11] Further processing of equation (1) yields the fit equation in SAS coordinates.

$$\frac{\Sigma_P}{\cos\theta}\sum_{i=1}^{n_x} a_i G_i - (\Sigma_H - \Sigma_P \tan\theta) b_0 + c_0 + c_1 x \cos\theta = H_y \cos\theta - H_x \sin\theta - \frac{\Sigma_P E_{0_x}}{\cos\theta} \tag{2}$$

where $(\Sigma_P, \Sigma_H, H_x, H_y, E_{0_x}, x, \theta)/(a_i, b_0, c_0, c_1)$ are the ALADYN input/output data. The order, n_x, of the series expansion in Legendre polynomials, G_i, depends on the precipitation profile, and increases when the precipitation (and polarization) scale size decreases.

[12] The input data set consists of: the Pedersen and Hall conductances, Σ_P, Σ_H, the magnetic field perturbation at ionospheric level (expressed in A/m and related to the field-aligned sheet current), H_x, H_y, the average ionospheric electric field, E_{0_x}, the satellite position, x, and the tilt of the arc/current sheet, θ. For nightside passes (as below) the conductance of the dark ionosphere is induced essentially by particle precipitation, and derived according to the formulas provided by *Robinson et al.* [1987] for electrons, and by *Galand and Richmond* [2001] for protons.

$$\Sigma_P^e = \frac{40\overline{E}}{16 + \overline{E}^2}\Phi_E^{1/2}, \qquad \frac{\Sigma_H^e}{\Sigma_P^e} = 0.45\overline{E}^{0.85} \tag{3}$$

$$\Sigma_P^p = 5.7\Phi_E^{1/2}, \qquad \frac{\Sigma_H^p}{\Sigma_P^p} = 0.45\overline{E}^{0.3} \tag{4}$$

with Φ_E the energy flux, and $\overline{E}$ the average energy, computed as the ratio between the energy and number flux, $\overline{E} = \Phi_E/\Phi_N$.

[13] Following *Galand and Richmond* [2001], the total conductance is estimated by $\Sigma_{P,H} = \sqrt{\sum_{P,H}^{e^2} + \sum_{P,H}^{p^2}}$. The components $H_{x,y}$ are computed from the magnetic field perturbation, $\Delta B_{x,y}$, measured by FAST, $H_{x,y} = m\Delta B_{x,y}/\mu_0$, with μ_0 the vacuum permittivity and m the linear mapping factor. The average ionospheric electric field, E_{0_x}, is obtained as the ratio of the potential drop along the satellite path to the length of the satellite path ionospheric footprint, with the potential drop computed by integrating the electric field component parallel to the satellite velocity.

[14] The output provided by ALADYN consists of the polarization coefficients, a_i, the longitudinal electric field, $E_{\eta} \equiv b_0$, the meridional current constant, c_0, and the electrojet divergence, c_1. Subsequently, one can compute the ionospheric electric field and current along the satellite footprint.

$$\begin{aligned} &E_x = E_{0_x} + \sum_{i=1}^{n_x} a_i G_i, \quad E_y = E_x \tan\theta + b_0/\cos\theta \\ &J_x = \Sigma_P E_x - \Sigma_H E_y, \quad J_y = \Sigma_H E_x + \Sigma_P E_y \\ &J_{\xi} = J_x \cos\theta + J_y \sin\theta, \quad J_{\eta} = -J_x \sin\theta + J_y \cos\theta \end{aligned} \tag{5}$$

The ionospheric potential obtained by integrating E_x can be compared with the potential based on the measured electric field, thus providing a cross-check of the results. The meridional and longitudinal currents, J_{ξ}, J_{η}, together with the divergence coefficient, c_1, and the field-aligned sheet current, $H_{\eta} = -H_x \sin\theta + H_y \cos\theta$, allow for the investigation of the 3D current closure along the satellite ionospheric footprint.

[15] As already mentioned, although ALADYN was initially developed in order to investigate arc electrodynamics (on latitudinal scales typically below 100 km), it can also be used to address larger scales. By properly dividing the examined interval into subintervals, one can check the auroral electrodynamics over the latitudinal extent of the electrojets, of the R1/R2 currents, or of the complete oval. The data events in the next Section illustrate the use of ALADYN on both arc and oval scales, while the limitations of the method and the precautions to be taken are detailed in section 5.1.

3. FAST Observations

[16] The development of the ALADYN method was stimulated by the examination of an arc event, presented here as Event 1, with conjugate FAST and ground optical observations. Although, at first sight, both the satellite and ground data seem to indicate a standard arc, the arc electrodynamics cannot be understood in terms of the Boström Type 2 configuration. A closer look at the data shows that the arc, as well as most of the R1 current, are located poleward of the CR, therefore Region 0 (R0) downward current near the poleward cap boundary would be needed for the standard closure of the R1 current. However, essentially no R0 current is observed. The detailed investigation made possible by ALADYN confirms that for Event 1 the FAC closure is essentially achieved by coupling with the electrojets. The upward R1 current is fed by a relatively strong WEJ poleward of the CR, while the downward R2 current feeds a weaker EEJ equatorward of the CR. The (latitudinally shifted) overlap of the WEJ and EEJ, the location of most of the R1 current poleward of the CR, and a ~10 mV/m westward electric field (inferred both from the optical data and ALADYN), indicate the location of Event 1 in the HR.

[17] The arc published by *Janhunen et al.* [2000], observed during FAST orbit 8707, offers an ideal "standard" case, to be compared with the atypical Event 1. This arc, presented here as Event 2, was located rather far from the CR, in the equatorward part of the oval, and was shown by *Janhunen et al.* [2000] to behave as a standard evening arc. A comprehensive set of ground optical, radar, and magnetic data from

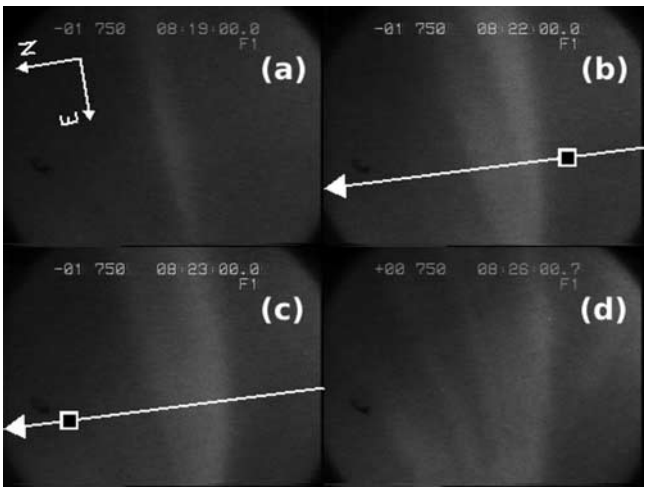

Figure 3. Ground optical data (a) before, (b, c) during, and (d) after the conjunction with FAST. The satellite footprint is indicated with a square in Figure 3b and 3c. Except for a ~200-m/s southward drift, the auroral structure is stable during the 2-min FAST overpass. On a ~10-min timescale, there is a clear development of the single arc (a) into a multiple arc system (d).

the MIRACLE network provides additional useful information. In good agreement with *Janhunen et al.* [2000], we find below that the current closure at and near the arc is achieved in the standard way, with a downward current equatorward of the arc feeding an upward current above the arc through a meridional Pedersen current. However, the application of ALADYN poleward of the arc reveals again that the upward FAC there is mostly closed in the longitudinal direction. Although the arc electrodynamics follows, in this case, the standard pattern, the oval electrodynamics bears similarities with those identified for Event 1: a fraction of the upward R1 current is fed by the WEJ while, by necessity, a fraction of the downward R2 current feeds the EEJ. As before, a key element for the current topology on oval scale is the relative location of the CR with respect to the FR. Even if the distance between the FR and CR is now fairly large, there is still substantial upward FAC poleward of the CR, not completely balanced by the (this time present) downward R0 current.

3.1. Event 1: FAST Orbit 1859

3.1.1. Event 1 Data

[18] The data for the first event were collected on 9 February 1997, around 8:22 UT, 21 MLT, by the FAST satellite [*Pfaff et al.*, 2001, and references therein] and a conjugate low-light TV camera [*Frey et al.*, 1996], located at Deadhorse, in northern Alaska (Lat. 70.22°, Lon. 211.61°). The camera was equipped with wide-angle optics (86° × 64°) and a ≥650-nm filter. The auroral ionosphere was relatively quiet before 9:00 UT, as witnessed by an AE index of ≲100 nT, ground magnetograms from Barrow and College, and Polar UVI images (not shown). Shortly before 9:00 UT a modest substorm started, with AE ≲ 300nT. Locally, the optical data at Deadhorse (Figure 3) show that between 8:19 and 8:26 UT a single arc develops into a multiple arc structure. Around the conjunction time (frames b and c) the arc structure is wide (~70-km), stable, moderately bright, and moves southward at a speed of ~200-m/s. The evolution visible in the optical data is consistent with a local activation shortly after the FAST overpass, during the growth phase of the substorm.

[19] A summary of the data measured by FAST, from subauroral latitudes up to the polar cap, is presented in Figure 4. During this time the satellite was close to apogee, at about 4000-km altitude. At the poleward side of the auroral oval, the visible arc is embedded in a large inverted-V (Figure 4a), whose most energetic part ($\overline{E} \lesssim 5$ keV, $\Phi_E \lesssim 10$ mW/m^2) is encountered above the arc. The inverted-V encompasses several ion beams (Figure 4b), indicating repeated passes through the lower part of the auroral acceleration region. The ionospheric conductance in the inverted-V region, from 8:22:00–8:23:20, is induced essentially by electron precipitation, and reaches maxima of 15 mho (Σ_P, Figure 4c), respectively 25 mho (Σ_H, Figure 4d). From about 8:20:00–8:22:00 the conductance has values ≲5 mho and the proton precipitation makes a substantial contribution to it. Before 8:20:00 and after 8:23:00 the particle precipitation becomes too weak for the application of equations (3) and (4).

[20] The large-scale trend of the ionospheric convection can be discussed on the basis of the electric potential (Figure 4f). The high-altitude potential (black line) was evaluated by integrating the measured electric field (Figure 4e) along the satellite track. It reaches a broad maximum at 8:20:00, indicating the corotation boundary, and an abrupt minimum shortly after 8:22:00. The ionospheric potential (magenta line) is based on the integration of the ionospheric electric field obtained by ALADYN (see section 3.1.2). The application of ALADYN was possible only between 8:20:30 and 8:23:00, when the conductance is high enough and the equations (3) and (4) provide reliable results. The high-altitude and the ionospheric potential agree quite well, except for the time intervals when ion beams are observed, because at such times the magnetic field line is no longer equipotential. The ionospheric potential reaches a sharp minimum at 8:22:04, which indicates the CR boundary.

[21] The magnetic field data (Figure 4g) shows the standard large-scale evening profile, with downward R2 (before 08:21:48) and upward R1 FAC sheets, essentially balanced and oriented roughly in E–W direction. The maximum value of ΔB_y, indicating the FR, is reached at 8:21:48. An outstanding feature of the data is the close proximity of the FR to the CR. It is just in the narrow strip between these two boundaries that the poleward electric field can drive a Pedersen current able to provide the standard connection between the downward and upward FAC. However, the FAC that leaves the ionosphere within this strip is just a small fraction of the total upward FAC. The Hall current that crosses the CR is rather small, because of the low conductance there, and it can supply just another small fraction of the upward FAC. Consequently, most of the upward FAC has to be fed by the WEJ, while most of the downward FAC feeds the EEJ. These qualitative considerations will be substantiated next by quantitative estimates.

3.1.2. Event 1 ALADYN Results

[22] ALADYN was applied between 8:20:30 and 8:23:00, a time interval of 2.5 min that corresponds to about 420-km ionospheric footprint or 4° latitude. A summary of ALADYN

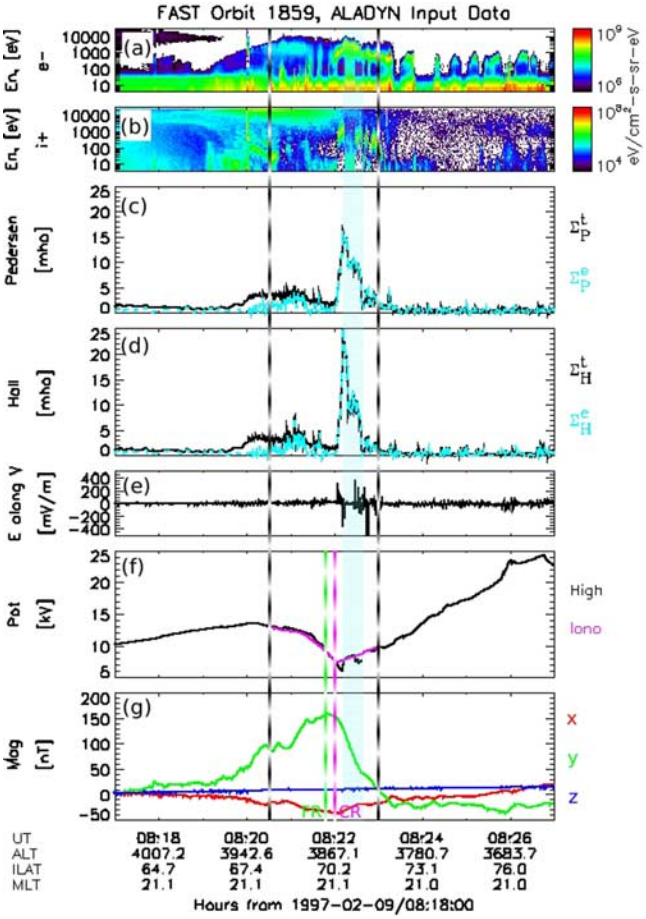

Figure 4. Selection of FAST particle and field data, used directly or indirectly by ALADYN. From top to bottom: (a) electron and (b) ion energy spectrograms; (c) Pedersen and (d) Hall conductance; (e) high-altitude electric field parallel to the satellite velocity; (f) high-altitude potential drop along the satellite track; (g) perturbation magnetic field. In Figure 4c and 4d the total/electron conductance is shown black/cyan. The quantities used directly by ALADYN are shown in double size panels. The dashed vertical lines indicate the ALADYN application interval, 8:20:30–8:23:00 UT. The visible arc is shown with the cyan band. The dashed magenta and green lines in Figure 4f and 4g indicate the CR and FR, respectively.

input data and results is presented in Figure 5: the Pedersen and Hall conductance (Figure 5a); the ionospheric electric field, E_x, as obtained by assuming a divergent ($c_1 \neq 0$), respectively divergence free ($c_1 = 0$) electrojet (Figure 5b); the associated potentials, together with the high-altitude potential (Figure 5c); the meridional (Figure 5d) and longitudinal (Figure 5e) current, J_ξ and J_η, together with their respective Pedersen and Hall components, as well as the field-aligned sheet current, H_η (Figure 5d). The currents J_ξ and J_η are shown only for the case $c_1 \neq 0$, when the match between the high-altitude and ionospheric potential is better. The average angle used for the AAS rotation with respect to the SAS was $\theta = 7.5°$. The precise value depends on the interval selected for minimum variance analysis, but the results are rather insensitive to small changes.

[23] The application of ALADYN before 8:20:30 and after 8:23:00 was not possible, because of uncertain conductance values. As visible in the ion spectrogram (Figure 4b), before 8:20:30 the proton precipitation energy overcomes the upper limit of the ion spectrometer, therefore our estimate is lower than the actual conductance. ALADYN compensates the missing conductance with an electric field stronger than the real one, which results in a mismatch between the ionospheric and the high-altitude potential (not shown). As already mentioned, after 8:23:00, the particle precipitation becomes very weak, and equations (3) and (4) are no longer accurate. The wrong conductance is compensated again by a

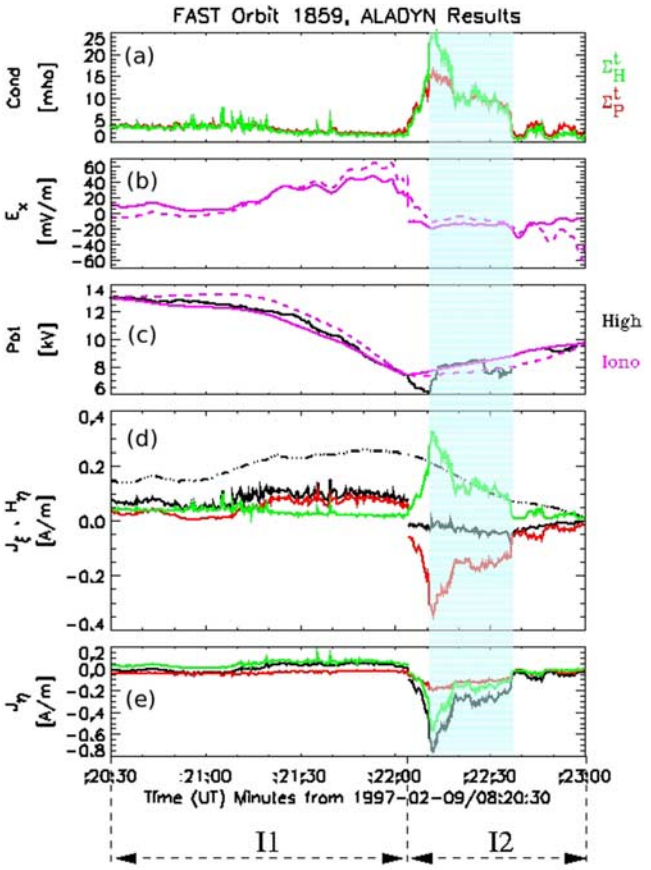

Figure 5. Electrodynamic parameters from 8:20:30–8:23:00. ALADYN was applied separately over the subintervals I1 and I2, equatorward and poleward of the CR. The quantities from top to bottom: (a) Pedersen and Hall conductance; (b) ionospheric electric field E_x obtained for $b_0 = -12$ mV/m and a divergent ($c_1 \neq 0$, solid), respectively divergent free ($c_1 = 0$, dashed) electrojet; (c) ionospheric potential (magenta, same line styles as in Figure 5b) and high-altitude potential (black); (d) ionospheric current J_ξ (black, solid), together with its Pedersen (red) and Hall (green) components, as well as the field-aligned sheet current, H_η (black, dash-dotted); (e) J_η current, same colors as J_ξ. The currents J_ξ and J_η are shown only for the case $c_1 \neq 0$, where the match between the ionospheric and high-altitude potential is better. The discontinuity in E_x (as well as J_ξ and J_η) between I1 and I2 reflects the sharp convection reversal. As in Figure 4, the cyan band indicates the visible arc.

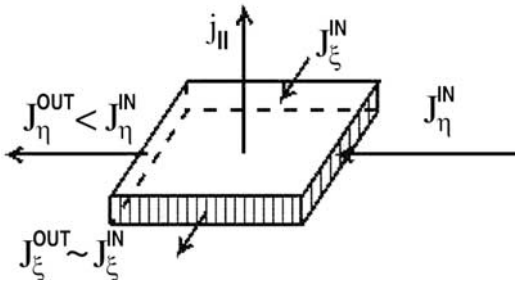

Figure 6. Illustration of the current continuity over interval I2, with the WEJ feeding the upward FAC.

wrong electric field, and the ionospheric potential does not match the high-altitude potential.

[24] The time interval where the conductance estimate is good enough was divided in two subintervals, I1 = 8:20:30–8:22:04 and I2 = 8:22:04–8:23:00, equatorward and poleward of the CR. A good consistency of the results was obtained only with divergent electrojets, a divergent EEJ over I1 and a divergent WEJ over I2. In this case, if b_0 is fixed at 12 mV/m westward, the derived E_x integrates to a potential in good agreement with the high-altitude potential both on I1 and I2. The value of b_0 is consistent with the estimate of about 10 mV/m based on the arc motion visible in the optical data. When the EEJ and WEJ are allowed to diverge, E_x is discontinuous between I1 and I2, reflecting correctly the sharp convection reversal. On the contrary, when the electrojets are forced to be divergence free, the electric field at the CR is almost continuous, since the current fed by the downward current can only be transported away across the CR. Therefore the CR appears to be smooth in this case, inconsistent with the data.

[25] When b_0 is free to vary, the unconstrained fit over I2 provides consistent b_0 values, of 10–12 mV/m, depending slightly on the right limit of I2. The situation is different over I1, where the unconstrained fit (not shown) results in an ionospheric potential that does not match the high-altitude potential. In addition, the unconstrained fit yields b_0 positive (eastward E_η), implying a discontinuity in the longitudinal electric field. Over I1, only a constrained fit provides consistent results, indicating that E_η is essentially "forced" from the magnetosphere. A similar conclusion was reached by e.g., *de la Beaujardière et al.* [1977], on the basis of radar observations. The consistency of the unconstrained fit over I2 suggest that the ionosphere there is in "equilibrium" with the magnetosphere. It would be interesting to check, but beyond the scope of this study, whether such an equilibrium is met more often near the poleward boundary of the oval, connected with the plasma sheet boundary layer, than at lower latitudes, connected with the inner plasma sheet.

[26] A key feature in Figure 5 is exhibited by Figure 5d, which shows that J_ξ cannot provide the ionospheric connection between the downward and upward FAC. The results are obtained for a neutral wind velocity of 160 m/s, that cancels the rotation of the Earth, but the variation of the neutral wind velocity does not change the basic results. As anticipated, J_ξ almost vanishes near the CR, and remains small in rest. Over I2, it is clearly visible that J_ξ does not follow the variation of H_η, therefore the meridional FAC closure can only play a minor role. Over I1, the correlation between J_ξ and H_η is better, indicating that the standard FAC closure is occasionally important. However, as discussed below, because of the decoupling at the CR between the large-scale downward and upward FAC, eventually most of the downward FAC can only feed the EEJ.

[27] The Pedersen and Hall components of J_ξ almost cancel each other over I2, a feature typical for a Cowling channel. However, in this case the meridional electric field shows little variation between the inside and outside of the arc, except for the localized enhancements at the arc edges. The polarization electric field, essential for a Cowling channel, is basically missing inside the arc, and its role is played by the background electric field oriented equatorward. Thus the arc is not a Cowling channel, although it appears to behave so, with J_ξ quite small and J_η substantial.

[28] The divergence coefficient c_1 was found to be about 0.4 μA/m^2 for the EEJ over I1, and -1.5 μA/m^2 for the WEJ over I2. These values imply total currents, $c_1 \Delta x \cos\theta$, roughly equal to 0.1 A/m over I1 and 0.2 A/m over I2, fed by the downward FAC to the EEJ, and by the WEJ to the upward FAC, respectively. Note the appropriate sign, positive over I1, where the electrojet intensity increases, and negative over I2, where the electrojet intensity decreases. In both cases, the integrated divergence of the electrojet is roughly equal to the current carried into or out of the ionosphere by the field-aligned current, which provides the quantitative proof for the FAC-EJ coupling.

[29] One should not forget, however, that the parametrization of the electrojet divergence with the constant coefficient c_1 is a very simple one, and it can only capture the average behavior over a certain time interval. In our case, the slope of H_η is not constant over I1, which shows that $j_{||}$ varies, therefore the fine structure of the FAC closure over I1 requires also the contribution of J_ξ. Over I2, the slope of H_η shows considerably less variation, indicating that not only the average, but also the fine structure of the current transfer is dominated by the FAC-EJ coupling. The little variation of J_ξ over I2 is consistent with this conclusion. The cartoon in Figure 6 illustrates the current closure over I2, with J_ξ essentially constant and J_η feeding the upward $j_{||}$. The limitations of ALADYN, as well as possible cures, are discussed in more detail in section 5.1.

[30] In summary, we found a strong WEJ north of the CR, which feeds the upward FAC, and a weaker EEJ south of the CR, fed by the downward FAC. The FAC-EJ coupling in the WEJ region is essentially local, while in the EEJ region part of the coupling is local, while another part is remote, with the FAC current diverted first in meridional direction. A minor fraction of the downward FAC, of $\sim$0.03 A/m, crosses the CR as Hall current to join the westward electrojet. Just a negligible part of the downward FAC, $\sim$0.01 A/m, is connected to the upward FAC between the FR and CR, which indicates that the R1 and R2 currents are essentially decoupled in ionosphere, in the vicinity of the FAST footprint.

3.1.3. Event 1 Discussion

[31] Current closure in the HR is notoriously complicated. *Koskinen and Pulkkinen* [1995] suggested that the HR current topology lies somewhere between two extremes: (1) A sharp discontinuity, with strong shear in the plasma flow, and Pedersen currents feeding an intense upward FAC from both sides of the discontinuity, during, e.g., the sub-

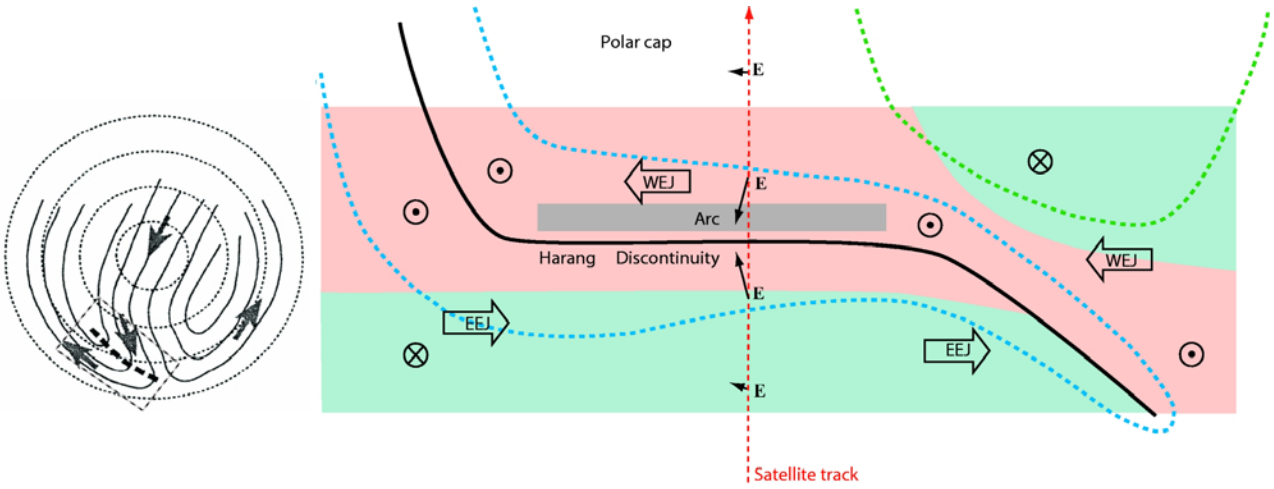

Figure 7. (left) Schematic representation of the large-scale ionospheric convection, with the indication of the Harang discontinuity [after *Koskinen and Pulkkinen*, 1995]. (right) Blow-up of the convection and current pattern, which tries to match our observations to published features of the HR. The evening and morning convection cells are shown with blue and green dotted lines, respectively. The FAC is upward in the pink region and downward in the two green regions. The eastward and westward electrojets are indicated by the EEJ and WEJ arrows.

storm expansion phase. (2) A smooth discontinuity, with continuous plasma flow and weak or even missing FAC, during quiet conditions. While in the first case the current closure is dominated by the coupling between the FAC and the transverse Pedersen current, in the second case the current is closed essentially in the ionosphere, where a mix of Pedersen and Hall currents couples the EEJ with the WEJ. Our event illustrates a third corner point, where the current closure is dominated by the FAC-EJ coupling.

[32] A schematic representation of the arc and the HR nearby is given in Figure 7. The blowup on the right tries to match our data to published HR features. The plasma flow appears to be generally consistent with the schematic convection pattern indicated at the left [after *Koskinen and Pulkkinen*, 1995] and with the SuperDARN convection map at 8:20:00 UT (not shown). On a smaller scale, the current structure agrees with the sketch from Figure 9 of *Fontaine and Peymirat* [1996], in particular the upward current "throat" between the two downward current regions. A good fraction of the sharp convection reversal (the "Harang discontinuity" proper) is located at roughly constant latitude [e.g., *Nielsen and Greenwald*, 1979].

[33] In the context of past studies, it is interesting to compare our results with those obtained by *Fujii et al.* [1994], in a study addressing the electrodynamics of the nighttime auroral oval during substorms. The magnetic and electric field data from Figure 6 of *Fujii et al.* [1994] are, in some respects, similar to ours, with the R1 upward FAC poleward, and the R2 downward FAC equatorward from the CR. Although part of the R1 current is closed by downward R0 current (missing in our case), the data suggest that the FAC-EJ coupling plays an important role in closing the rest of R1 and the R2 current. However, these data are observed during a substorm, and associated with the "Middle Surge" sector of the auroral bulge, according to the classification of *Fujii et al.* [1994]. Under these conditions the FAC-EJ coupling, probably associated with the ionospheric closure of the substorm current wedge, is not very surprising. The association with the substorm current wedge is well supported by the rather complicated magnetic field data, not consistent with the standard signature of a current sheet. Unlike the configuration of *Fujii et al.* [1994], in our event both the magnetic field and the optical data suggest the standard current closure. In addition, our data are observed during the growth phase of a substorm, when the current wedge is not supposed to have formed yet. Despite this expectation, the experimental evidence presented above seems to indicate that a precursor of the current wedge is already in place during the growth phase, a topic to be discussed further in section 5.3.

3.2. Event 2: FAST Orbit 8707

3.2.1. Event 2 Data

[34] The satellite and ground data associated with FAST orbit 8707 are described in detail by *Janhunen et al.* [2000]. In this Section we shall only point out a number of features important for the application of ALADYN and for the interpretation of the results. For easy comparison with Event 1, we present here in Figure 8 the ALADYN input data provided by FAST, in a format similar to Figure 4. Note that unlike in Figure 4, the FAST motion is now equatorward, and the orientation of the SAS and AAS coordinates is opposite to that in Event 1: the axes x and ξ point roughly to the South, while y and η roughly to the West.

[35] The optical and STARE radar data are presented in Figures 4 and 5 of *Janhunen et al.* [2000], and not repeated here. The optical data indicate a ~40-km wide, elongated, and stable arc, encountered by FAST as inverted-V electron precipitation from 17:36:11–17:36:18 UT (Figure 8a). The optical data show as well that another inverted-V interval, 17:35:35–17:35:45 UT, is not associated with an arc but rather with a precipitation blob. The radar data indicate that the plasma motion is parallel to the arc, implying a purely

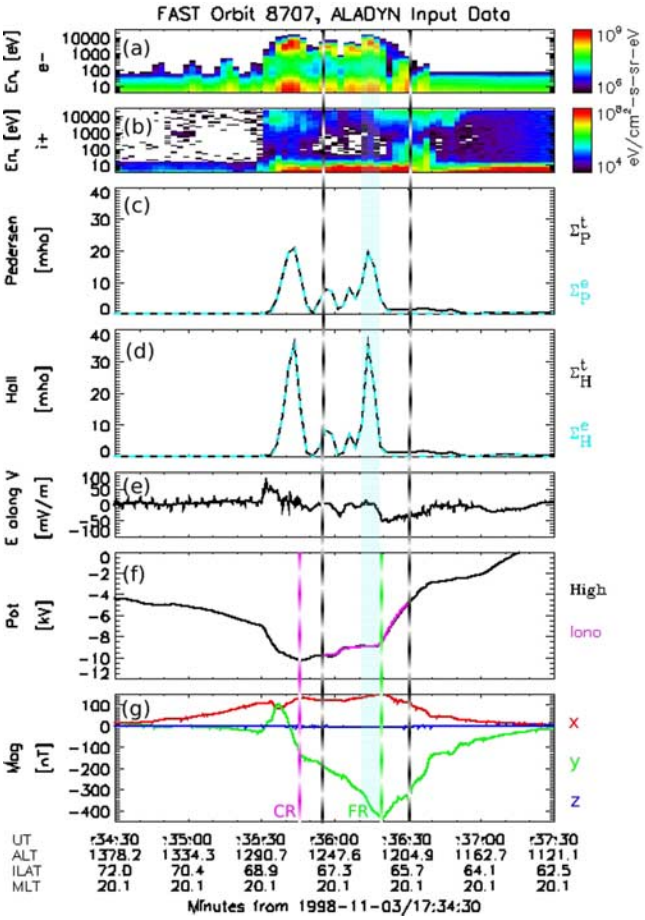

Figure 8. Selection of FAST particle and field data for orbit 8707, in a format similar to Figure 4. The ALADYN application interval is now 17:35:55–17:36:30. As compared to orbit 1859, the CR, at 17:35:45, is no longer close to the FR, at 17:36:18, but still embedded in the upward R1 current.

meridional electric field. The lack of a longitudinal electric field is a useful constraint for ALADYN, by setting $b_0 = 0$.

[36] As reported by *Janhunen et al.* [2000], the level of magnetic activity read in the magnetograms of the IMAGE network is low ($\lesssim$100 nT). At the same time, the AE index (not shown) indicates a rather disturbed auroral oval, at the maximum epoch of a moderate substorm ($\lesssim$500 nT). This is consistent with the extension of the HR deep in the evening sector, as early as 20 MLT, the local time of the FAST observations.

[37] Two data signatures are typical for the Harang region: First, the overlap of the EEJ with a poleward shifted WEJ, resulting in this case from the electric field peak after 17:35:30 UT (Figure 5e) and the conductance peak around 17:35:40 UT (Figure 5d). Also, second, the downward current at the poleward edge of the oval, from roughly 17:35:30–17:35:35 (Figure 5g). Unlike for Event 1, where the magnetic field exhibited a standard R1/R2 configuration at 21 MLT, this time a third, R0 sheet is present at 20 MLT. The difference is consistent with the geophysical conditions: while Event 1 was associated with the growth phase of a small substorm, Event 2 is observed at the maximum epoch of a moderate substorm. The FAC intensity is also consistent: while the mapped magnetic perturbation for Event 1 reaches a maximum of $\sim$300 nT, for Event 2 it goes up to $\sim$550 nT (absolute value).

[38] Unlike for Event 1, where the arc was poleward and close to a sharp CR, this time the arc is equatorward and rather far from a considerably smoother CR (Figure 5f). The FR is also far from the CR, nonetheless there is substantial R1 upward current poleward of the CR, not completely balanced by the R0 downward current. A priori, we expect to find the standard current system at and around the arc, but a certain divergence of the longitudinal current and coupling with the FAC near the CR (here we refer to the 'longitudinal current' rather than the 'electrojet' because of the very weak

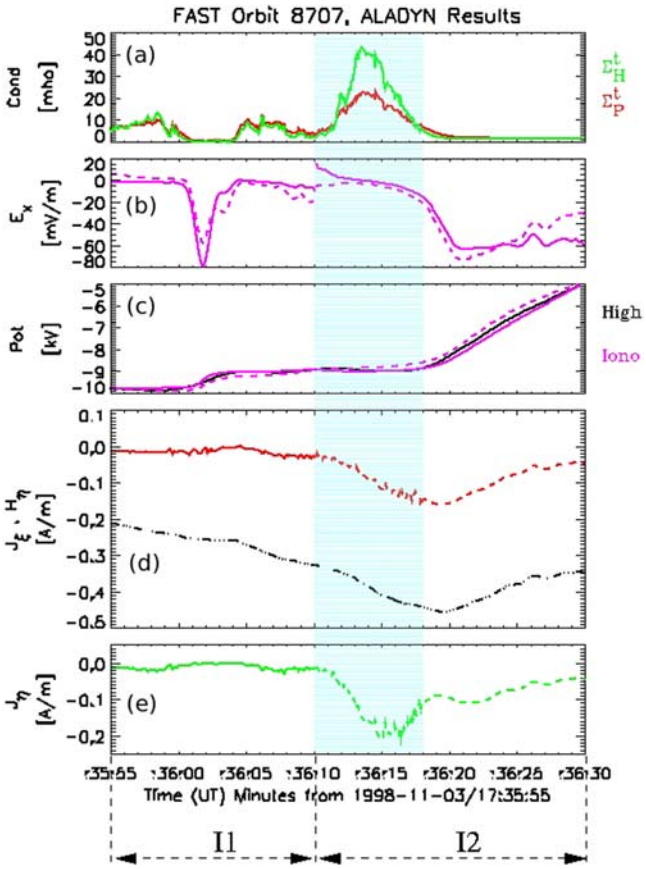

Figure 9. Ionospheric parameters for FAST orbit 8707, from 17:35:55–17:36:30, in a format similar to Figure 5. ALADYN was applied again on two subintervals, I1 and I2. Unlike in Figure 5, since $E_\eta = 0$, J_ξ has only the (red) Pedersen component and J_η the (green) Hall component. In Figure 9d and 9e we show only the currents obtained with $c_1 \neq 0$ over I1 (solid) and $c_1 = 0$ over I2 (dashed), when the results are more consistent. Compared to Figure 5, the match between the ionospheric and high-altitude potential in Figure 9c is now quite good, irrespective of the model, both over I1 and I2. In order to select the better model, we note that E_x in Figure 9b is continuous between I1 and I2, in agreement with the smooth profile of the high-altitude potential, only when $c_1 \neq 0$ over I1 and $c_1 = 0$ over I2.

current intensity). As before, we shall substantiate these qualitative conclusions by quantitative ALADYN results.

3.2.2. Event 2 ALADYN Results

[39] The ALADYN application interval for Event 2, I = 17:35:55–17:36:30 UT, does not include the CR any more, as for Event 1. The consistency check, based on the matching of the high-altitude and ionospheric potential, becomes worse when trying to extend the application interval. At higher latitudes, the longitudinal homogeneity near the precipitation blob is no longer a reasonable assumption. At lower latitudes, the conductance estimate is not good enough, because we underestimate the proton contribution. As visible in Figure 8b, the high-energy protons are cut off, and the underestimation of the conductance starts to be significant after 17:36:30, when the proton contribution becomes dominant.

[40] The results obtained by ALADYN are summarized in Figure 9, using the same layout as in Figure 5. The average tilt of the FAC sheets was $\theta = 14°$ and, as for Event 1, no significant changes were observed when slightly different θ values were tried. With b_0 and c_1 constrained to zero over I, although the results (not shown) were in general consistent, we could not reproduce the intensification of the electric field around 17:36:02. In order to obtain fully consistent results we had to split the application interval in two subintervals, I1 = 17:35:55–17:36:10 and I2 = 17:36:10–17:36:30 (comparable results were obtained with I1 = 17:35:55–17:36:05 and I2 = 17:36:05–17:36:30). As discussed by *Janhunen et al.* [2000], the STARE electric field available south of the arc matches the FAST electric field, providing an additional cross-check for the ALADYN results.

[41] The best consistency was obtained when the longitudinal current was assumed divergent over I1 ($c_1 \neq 0$), and divergence free over I2 ($c_1 = 0$). However, as seen in Figure 9c, the match between the high- and low-altitude potential is now about equally good, irrespective of the model used. Therefore this criterion is less conclusive than for Event 1. The main evidence in favor of the selected models is that this is the only choice rendering E_x continuous at the boundary between I1 and I2. Note that unlike in Event 1, this time the potential there is smooth, therefore E_x is indeed expected to be continuous.

[42] Consequently, within I2, the downward current equatorward of the arc is continued by a Pedersen current normal to the arc and closed by an upward current above the arc, consistent with Figure 6 of *Janhunen et al.* [2000]. Figure 9d illustrates this standard current closure by the good match between the profiles of H_η and J_ξ over I2. Poleward of the arc, within I1, the current continuity is achieved, to a good extent, at the expense of the divergence in the J_η current, with $c_1 \simeq -1.1$ μA/m^2. Because of the very small longitudinal current (Figure 9e), one cannot speak about an electrojet there. However, since the average upward FAC density over I1 (computed as $-\Delta B_y/\mu_0 \Delta x$) is $\sim$1.3 μA/m^2, comparable to c_1, it appears that *on average* the upward FAC is closed in the ionosphere in the longitudinal rather than meridional direction. Because c_1 is a quite sensitive parameter, as already pointed out with respect to Event 1, we tend to be cautious about its exact numerical value, but we trust that this value is negative and significant. We also note that our rough estimate of the FAC density above is consistent with Figure 3 of *Janhunen et al.* [2000], which shows values slightly above 1 μA/m^2 over I1, when determined from the magnetic field data.

[43] Although the lack of a good conductance estimate at the south and the deviation from the arc geometry at the north prevent us to apply ALADYN there, a qualitative exploration of the current closure is still instructive. By moving with FAST from the poleward boundary of particle precipitation, at 17:35:30, to the CR boundary, at 17:35:45, there is a net upward FAC, corresponding to a decrease in ΔB_y of 120 nT (Figure 8g). Assuming a current sheet geometry and a linear mapping factor m = 1.25, the equivalent current is $m\Delta B_y/\mu_0 \simeq 0.12$ A/m. Since the sheet geometry is not supported by the optical data, the accuracy of this result is questionable. However, we believe that the qualitative result is correct, namely the presence of a net upward current poleward of the CR. This current cannot be fed through the CR, where both E_x and E_y are zero, and cannot come from the polar cap, where the conductance is too low. Therefore it only remains that the excess upward current is supplied by the WEJ. In a similar way, south of the CR, until 17:37:30, there is a net influx of $\sim$0.12 A/m downward current, which can only feed the EEJ.

[44] To conclude this Section, it is interesting to repeat the comparison with *Fujii et al.* [1994], which can be done more properly than for the first event, since the observations occur at the maximum epoch of a substorm. According to the classification of *Fujii et al.* [1994], Event 2 appears to be located in the "Surge Horn", and the data in Figure 8 have similar features with those identified by *Fujii et al.* [1994] for this sector. However, while the overall FAC balance is interpreted by *Fujii et al.* [1994] in terms of meridional FAC closure, our analysis suggests that the current configuration is more complicated.

4. Synthetic Data

[45] In the following we shall explore the relative location of the CR and FR, as well as the CR profile, by synthetic data. Anticipating the results, the most important parameter is the westward component of the electric field, while the conductance and FAC structure around the FR contribute to shaping the CR profile.

[46] The setup to be explored consists of a balanced pair of large-scale FAC sheets, each of them carrying an integrated current of $\sim$0.12 A/m at ionospheric level, and an average poleward electric field of 5 mV/m, over an oval width of 500 km. Σ_P and Σ_H are constant over the downward and upward FAC branches, with higher values for the upward current. In order to investigate the role of the conductance gradient we examine two cases, (1) with Σ_P = 3/7 mho and (2) with Σ_P = 3/60 mho for the downward/upward current region. The ratio Σ_H/Σ_P is in both cases equal to 0.8 over the downward FAC and to 1.5 over the upward FAC. The transitions between the different regions are rather abrupt, with little smoothing in the conductance and FAC profiles, resulting in abrupt variations of E_x. More realistic profiles of E_x could be obtained by adjusting the smoothing, however this has no essential influence on the results.

[47] In our simple configuration, with constant conductances for the upward/downward current regions and a sharp

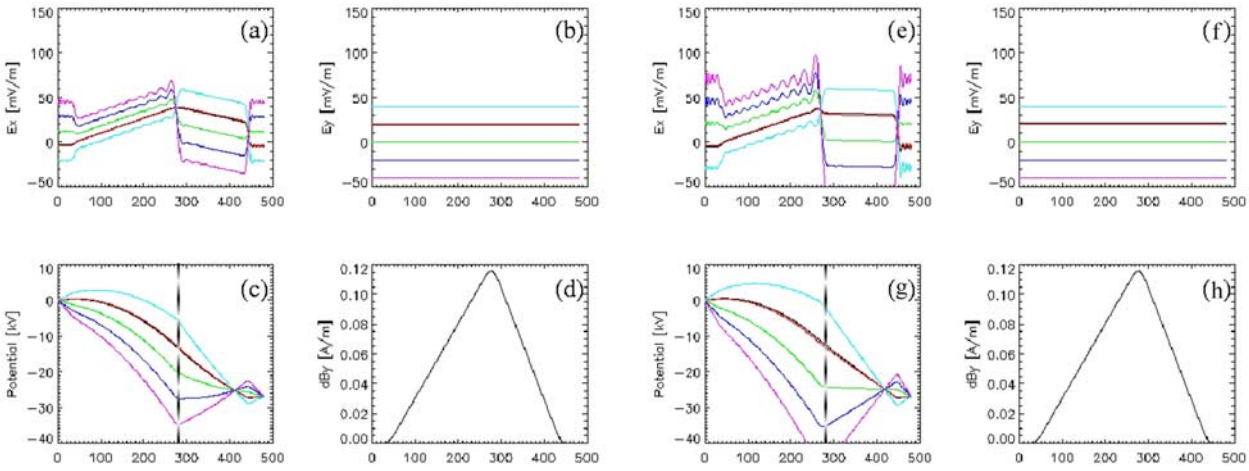

Figure 10. Results obtained with synthetic data for a large-scale pair of downward/upward FAC sheets, with (a–d) $\Sigma_P = 3/7$ mho and (e–h) $\Sigma_P = 3/60$ mho. We show E_x (Figures 10a and 10e), E_y (Figures 10b and 10f), the potential corresponding to E_x (Figures 10c and 10g), and H_y (Figures 10d and 10h), for E_{0_x} = 5 mV/m. The integrated FAC current into the ionosphere reaches a maximum of ~0.12 A/m at the FR and is balanced to 0 at the end of the interval. The dashed vertical lines in Figures 10c and 10g indicate the FR. In our simple model, if E_y is negative enough, the CR "jumps" from the poleward boundary of the FAC region to the FR (see text). The ratio Σ_H/Σ_P is 0.8/1.5 over the downward/upward FAC region. The background conductance outside of the FAC region is 2 mho. The average divergence coefficient, c_1, is assumed to be zero. $E_y \equiv b_0$ is constrained to −40 mV/m (magenta), −20 mV/m (blue), 0 mV/m (green), 20 mV/m (red), and 40 mV/m (cyan). The black line (almost on top of the red line) shows the result of the unconstrained optimization, where b_0 is free to vary as well.

conductance gradient at the FR, it is not possible to model the gradual shift of the CR toward the FR. Depending on the magnitude of the longitudinal electric field and on the conductance gradient, the meridional electric field can become negative poleward of the FR, which translates into a "jump" of the CR from the poleward boundary of the FAC region to the FR. More realistic conductance and FAC profiles would allow a gradual shift of the CR toward the FR, but the key influences on the CR location and profile are already visible with the simple model.

[48] The ionospheric electric field and potential, as obtained by ALADYN in the two cases, are presented in Figure 10. Since the average electrojet divergence is small on oval scale, because of compensating sources and sinks in different parts of the oval (in particular for a balanced FAC), we have used only divergence free models, with c_1 constrained to zero. In this case, if we assume, for simplicity, that $\tan\theta = 0$, and use only (x, y) coordinates, the fit equation (2) reduces to

$$\Sigma_P \sum_{i=1}^{n_x} a_i G_i - \Sigma_H b_0 + c_0 = H_y - \Sigma_P E_{0_x} \tag{6}$$

which is the integrated form of equation (1) when $c_1 = 0$

$$\frac{dJ_x}{dx} = j_{\parallel} => \Sigma_P \frac{dE_x}{dx} + \frac{d\Sigma_P}{dx} E_x = \frac{d\Sigma_H}{dx} E_y + j_{\parallel} \tag{7}$$

As pointed out by *Karlsson* [2001], if Σ_P, Σ_H, j_z, and $E_y \equiv b_0$ are known, equation (7) can be regarded as a first order differential equation in E_x, having a unique solution as soon as the value of E_x at a certain point is determined. Alternatively, one can use the more robust average value of E_x, as in the ALADYN applications. When b_0 is free to vary, the solution is no longer unique, and ALADYN operates an unconstrained selection in a one dimensional solution space. However, as already pointed out, this unconstrained selection may provide results in disagreement with the physical reality. This happens because the unconstrained selection misses the magnetosphere-ionosphere (M–I) coupling, which can force some of the parameters, notably b_0, to certain values, different from those based on a free optimization. For a given conductance pattern, the current continuity equation at ionospheric level does not have a unique electric field solution. The magnetosphere is able to "force" the selection of a "less convenient" solution from the ionosphere viewpoint, by imposing b_0.

[49] Figure 10 provides a convincing demonstration for the difference between the constrained and unconstrained optimization. The unconstrained optimization yields always a positive b_0 of ~20 mV/m (black lines), in disagreement with the observed behavior of E_y, which is often negative in the Harang region and about zero otherwise. The constrained optimization shows the variation of the potential from a typical early evening configuration, with the CR at the poleward boundary, to a HR configuration, with the CR deep within the oval, when b_0 becomes negative enough. The excursion of the CR toward the FR depends on the conductance gradient at the FR. If this gradient is moderate, as in case 1, a large negative b_0, of between 20 mV/m and 40 mV/m, is required. However, if the gradient is substantial, as in case 2, just a small b_0, of a few mV/m, is

enough to obtain a sharp CR in the close vicinity of the FR, resembling the configuration of Event 1. The exact profile of the CR is controlled by the small-scale structure of the FAC and conductance. In order to investigate a more realistic configuration we added a pair of small-scale FAC sheets first on the upward branch of the large-scale FAC and then on the downward branch. The results (not shown) indicate that a structured FAC and conductance pattern can be associated with a less sharp CR, resembling the configuration of Event 2.

[50] Although our synthetic data exercise is very simple, it clearly shows that the location of the CR is controlled by the longitudinal electric field, E_y, while its profile is shaped by the FAC and conductance pattern. A negative E_y pushes the CR toward the FR, and a steep conductance gradient results in a sharp CR. Complex FAC and conductance distributions can result in more complicated CRs, like double reversals. In the Harang region E_y is often negative, therefore it is not surprising to find the CR close to the FR. This configuration prevents the standard closure of the current and favors the FAC-EJ coupling. As a matter of fact, a CR location deep within the upward FAC region is another way of defining the Harang region. The presence of the WEJ requires substantial conductance poleward of the CR, which can only be provided by the electron precipitation associated with the upward FAC.

5. Discussion

[51] In this section we shall focus on three issues, only briefly touched upon so far. First, we shall discuss the limitations of the ALADYN method in its current implementation, as well as possible cures for some of these limitations. Next, we shall check closer the Hall and Pedersen contributions to the FAC-EJ coupling. Finally, we shall comment on the implications of the FAC-EJ coupling for the current closure in the equatorial magnetosphere and the auroral current circuit.

5.1. Limitations of the ALADYN method

[52] The accuracy of the ALADYN results depends on: (1) the accuracy of the input data, (2) the choice of the fit model, and (3) the selection of the fit interval.

5.1.1. Accuracy of the Input Data

[53] From our experience so far, the most sensitive parameter appears to be the conductance. As commented in section 3.1.2, in order to fulfill the fit equation (that is, the current continuity), a wrong conductance is compensated with a wrong electric field, which results in a mismatch between the observed and computed potential. As long as the particle precipitation is the dominant conductance driver, equations (3) and (4) yield reasonable estimates, provided that the average energy of the particles is above $\sim$1 keV. When the particle average energy and/or energy flux becomes too low, the formulas are no longer accurate. This happens, in general, when the conductance is low, typically in downward current regions, both on arc and oval scale. Wrong conductance estimates are also possible when the spectrometer does not cover the full range of particle energies, as illustrated with the proton population at the equatorward border of the oval. The accuracy of the conductance estimates could be improved by using, e.g., additional information from conjugate ground observations, when available. In such cases it would be interesting to combine ALADYN, able to provide high-resolution results along a 1D ionospheric cut, with standard ground techniques, that cover a 2D domain at lower resolution.

5.1.2. Choice of the Fit Model

[54] In the present implementation, a certain ability is required to decide whether the fit model should be constrained or not, and if yes, what should be the constraint(s). As already discussed, the M–I coupling can impose bounds on the ionospheric parameters, which are not properly taken into account by the unconstrained model. Both the longitudinal electric field, b_0, and the divergence of the electrojet, c_1, can take values different from those yielded by the unconstrained optimization. Currently, these values are found on a trial-and-error basis, an approach that will be replaced in the future with a systematic search in the parameter space.

[55] A basic limitation is the assumption of longitudinal homogeneity, associated with the use of cartesian coordinates. Preliminary tests suggest that ALADYN could be generalized to curvilinear coordinates, making possible the extension of the method to more complicated auroral forms.

5.1.3. Selection of the Fit Interval

[56] ALADYN does not take into account temporal variations, therefore the fit interval should be, in principle, short. As already pointed out, the assumption that c_1 is constant requires short intervals as well. Consequently, a longer time interval should be divided in a number of subintervals, and then ALADYN applied to each subinterval. However, in practice this is not an easy procedure, at least until the systematic search of the parameter space is implemented. More critical, the smooth transition of the parameters between the subintervals is not guaranteed. For example, if the boundary between two subintervals is located in a low-conductance region, where the conductance estimate is less reliable, the derived electric field is less reliable as well, and the chance to have a good match between the subintervals is problematic. Therefore a proper selection of the subintervals has to be ensured, which adds complexity to the already demanding task of choosing the appropriate fit model on each subinterval. Although in principle possible, the development of an integrated algorithm, able to optimize among the various constraints, appears as a rather difficult task.

5.2. Hall and Pedersen Contributions to the FAC-EJ Coupling

[57] The longitudinal variation of J_η and the FAC-EJ coupling can, in principle, be related to the variation of both the conductance and the electric field. Since by assuming that the electric field is constant in the longitudinal direction, our results were rather consistent, in the following we shall concentrate on the variation of the conductance. It is worth mentioning in this context the results of *Kamide and Kokubun* [1996], who suggested that during substorms the electrojet consists of two components, one of them related to the large-scale convection pattern and the other to the substorm current wedge (see in particular their Figure 11). The intensification of the first component, ''electric field dominant'', occurs mainly because of the increase in the electric field due to enhanced convection, directly driven from the solar wind. The second component, ''conductivity dominant'', is controlled by the increased precipitation in the

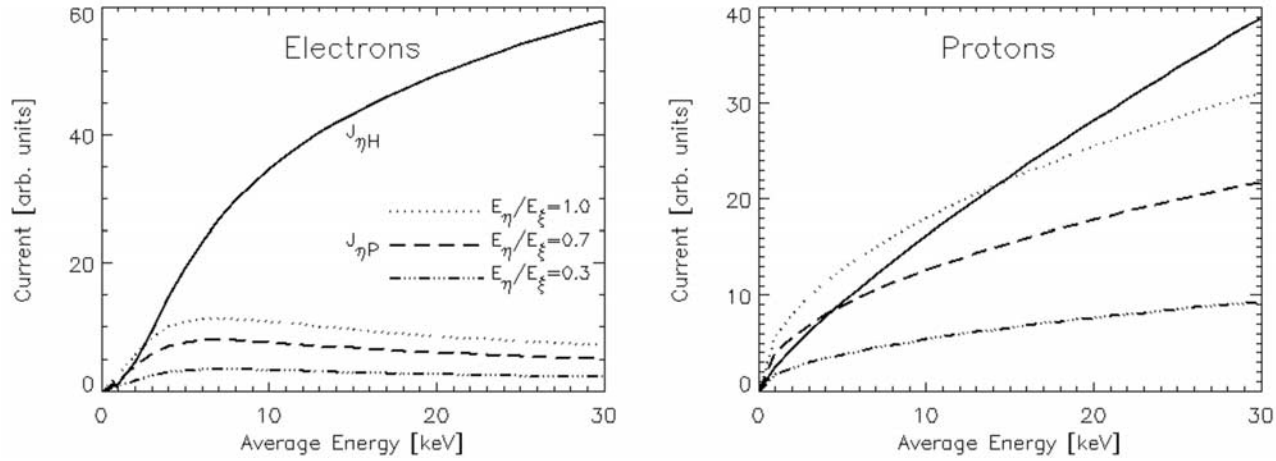

Figure 11. Dependence of the Hall and Pedersen components, $J_{\eta H}$, $J_{\eta P}$, of the longitudinal current (in arbitrary units) on the average particle energy. The Pedersen current is shown for three different ratios of the longitudinal to meridional electric field, E_η/E_ξ. In the HR, a conductance dominated by electrons is typical for the WEJ, while a conductance dominated by protons can be associated with portions of the EEJ. The particle flux (and the FAC density) is assumed to be constant in the longitudinal direction.

midnight sector due to accelerated electrons that unload magnetic energy from the tail. A direct comparison with the work of *Kamide and Kokubun* [1996] is not possible, because of widely different spatial and temporal scales. However, if the "Harang Discontinuity" in Figure 11 of *Kamide and Kokubun* [1996] is replaced by a less sharp "Harang Region", and if the Event 1 activation is seen as a localized unload, then our events appear to show "conductivity dominant" features.

[58] In the following, we shall assume that not only the electric field, but also the FAC is uniform in the longitudinal direction, consistent with the sheet geometry indicated by the magnetic field data. This implies that the particle flux, Φ_N, is uniform as well, and the conductance equations (3) and (4) can be rewritten as

$$\Sigma_P^e = \frac{40\overline{E}^{1.5}}{16+\overline{E}^2}\Phi_N^{1/2} \quad (8)$$

$$\Sigma_H^e = \frac{18\overline{E}^{2.35}}{16+\overline{E}^2}\Phi_N^{1/2} \quad (9)$$

$$\Sigma_P^p = 5.7\overline{E}^{0.5}\Phi_N^{1/2} \quad (8)$$

$$\Sigma_H^p = 2.6\overline{E}^{0.8}\Phi_N^{1/2} \quad (9)$$

With Φ_N constant, the only parameter left to account for the longitudinal change in conductance, and in the intensity of the electrojet, is the particle average energy, $\overline{E}$. Under these assumptions it becomes possible to check whether the FAC-EJ coupling is dominated by the Hall or by the Pedersen contribution, which makes a significant difference in the local energy balance, and has implications for the entire auroral current circuit.

[59] Figure 11 shows the variation of the Hall and Pedersen components of the electrojet, $J_{\eta H}$ and $J_{\eta P}$, with $\overline{E}$, both for the electron and proton induced conductance. A steep variation of the current indicates a large divergence of the electrojet and a substantial FAC-EJ coupling. The upper $\overline{E}$ limit of 30 keV covers the full energy range of auroral precipitation in most cases, and could be easily increased for extreme events, without essential changes in the discussion. The Pedersen current is computed for three different ratios of the longitudinal to the meridional electric field, E_η/E_ξ, equal to 0.3, 0.7, and 1, covering as well a wide spectrum of conditions.

[60] The FAC-EJ coupling depends both on the dominant particles, on the average energy, and on E_η/E_ξ (in particular for protons). When the electrons dominate, typically in upward FAC regions, the Hall current is seen to be the main responsible for the coupling at high energies, as expected in active regions during disturbed times. However, at energies of a few keV, during quiet intervals and substorm growth phase, the Pedersen current may also play a role, occasionally comparable to the Hall current. Even if the current associated with proton precipitation looks somewhat different, the Hall current is still the main contributor to the FAC-EJ coupling, since E_ξ is in general significantly larger than E_η. In addition, the average energy of the proton precipitation in the downward current region of the evening sector, where the proton induced conductance can dominate, is typically quite high, of $\sim$10 keV or more. However, again, as for the electrons, there are also possible regimes with comparable, or even larger Pedersen contribution to the coupling.

[61] In our Event 1 $E_\eta/E_\xi \lesssim 1$ over substantial fractions of both the upward and downward FAC regions, and the average electron energy is a few keV. Consequently, even if the Hall contribution to the FAC-EJ coupling is probably larger, the Pedersen contribution is significant as well, both poleward and equatorward of the CR. The situation is different for Event 2, where the meridional electric field is zero. Therefore in this case the coupling is realized essentially by the Hall current. Since the two events are observed at different stages of the substorm (and at different locations), the difference in the FAC-EJ coupling might be associated with global changes in the auroral current circuit. Although in

the next Section we shall briefly comment on the implications of the FAC-EJ coupling for the auroral current circuit, a systematic investigation of the FAC-EJ coupling during the substorm cycle is beyond the scope of this study.

5.3. Implications for the Auroral Current Circuit

[62] The two FAST events and the tests on synthetic data suggest that the coupling with the electrojet is a significant FAC closure mechanism in the HR, both equatorward and poleward of the CR. In principle, the FAC-EJ coupling, anticipated already by *Boström* [1964], is not so surprising. As reviewed by *Baumjohann* [1983], the FAC-EJ coupling is realized in both the large-scale convection and substorm electrojets. However, the prevailing view is reflected by the *Boström* [1964] Type 1 model, where the FAC-EJ coupling is associated with filamentary FACs and localized in the longitudinal direction. In our events the FAC appears to be sheet like, and the coupling is distributed in the longitudinal direction. In some sense, this configuration is a mix between Type 1 and Type 2, with the FAC-EJ coupling specific to Type 1 and the sheet geometry of the FAC specific to Type 2. Unlike for Type 1, where the electrojet is essentially Pedersen current, our FAC-EJ coupling is related mainly to the Hall component of the electrojet. Because of the substantial amount of upward current poleward of the CR, associated with the westward electric field, the FAC-EJ coupling might be a frequent feature in the Harang region. This coupling occurs on both arc and oval scales, and is realized not only in association with the substorm electrojet, but also during, e.g., the growth phase.

[63] A significant fraction of the auroral arcs, traditionally associated with the Type 2 configuration, is expected to be related to the Harang region and to substorm processes. Although a detailed examination is beyond the scope of this paper, it is interesting to explore briefly the consequences of the distributed FAC-EJ coupling for the complete auroral circuit, including its closure in the equatorial magnetosphere. The current topology in the ionosphere suggests azimuthal closure in the magnetosphere, with the EEJ connected to the ring current and the WEJ to the cross-tail current. The magnetospheric closure of the EEJ has the same sense as the ring current, and could contribute to the asymmetry in the dusk sector. On the other hand, the magnetospheric closure of the WEJ proceeds against the cross-tail current, and could contribute to the current disruption. Here we shall concentrate on the WEJ current circuit, more closely related to the substorm development.

[64] The magnetospheric closure in the WEJ circuit is consistent with the work of *Akasofu* [2003] (in particular his Figure 4), who suggests that the sudden growth of the WEJ at the substorm onset results in a related enhancement of the equatorial current, compensating the cross-tail current. Thus the dipolarization and current disruption are achieved naturally at the substorm onset. The whole process, which includes the brightening of the breakup arc, is powered by a dynamo in the equatorial plane. However, the configuration of *Akasofu* [2003] is also Type 2, with the downward current poleward of the upward current resembling an R0/R1 FAC pair (opposite to that shown in Figure 1). The WEJ is driven as Hall current by an equatorward electric field, E_ξ, and is divergence free except for the end points, where is connected by FACs to the equatorial plane. The Hall current is carried by the eastward motion of the electrons, which follows the eastward frozen-in plasma motion in the equatorial plane, associated with a $-V \times B$ inward electric field, E_r. The current closure in the meridional loop, J_r, is opposite to the electric field, providing thus the required generator, $E_r J_r < 0$, that powers the aurora, in particular the load in the ionosphere, $E_\xi J_\xi > 0$.

[65] Compared to the work of *Akasofu* [2003], the meridional loop is missing in our case. Since most of the time the WEJ is still dominated by the Hall component, as discussed in the previous Section, the ionospheric load is less important, and sometimes completely missing. The energy provided by the magnetospheric generator is carried by Poynting flux along the magnetic field lines, and converted into kinetic energy in the auroral acceleration region (AAR). Subsequently, the accelerated electrons collide with the particles in the ionosphere, and their energy is converted into random thermal motion. While, on a global scale, energy dissipation in the auroral ionosphere is dominated by the Joule heating [e.g., *Akasofu*, 1981], particle heating may occasionally prevail in the Harang region, or in other regions with significant FAC-EJ coupling. At the generator level, the eastward current, J_ϕ, is opposite to the dawn-dusk electric field, E_ϕ, associated with the inward plasma convection, therefore $E_\phi J_\phi < 0$, that is the generator is indeed there. Unlike in the work of *Akasofu* [2003], the eastward motion of the ionospheric electrons in the WEJ is decoupled from the magnetospheric plasma motion by the parallel electric field inside the AAR.

6. Conclusions

[66] High-resolution satellite measurements, together with ground data, provide at present a powerful tool for detailed investigations of arc and oval electrodynamics. The examination of two apparently standard events in the HR, by the recently developed ALADYN method, revealed that the ionospheric current closure was dominated by the FAC-EJ coupling over substantial fractions of the auroral oval. In the first event, during the growth phase of a small substorm, the CR and FR were located close to each other, and the large-scale upward and downward FACs were essentially decoupled near the ionospheric footprint of the satellite path. In this case, the WEJ was found to feed most of the upward FAC associated with a wide and stable auroral arc poleward of the CR, while the EEJ appeared to be fed by the downward FAC. In the second event, at the maximum epoch of a moderate substorm, the application of ALADYN to an auroral arc equatorward of the CR confirmed the standard configuration, consistent with the results of *Janhunen et al.* [2000]. However, the FAC-EJ coupling was demonstrated to be important in other parts of the auroral oval.

[67] Simple tests on synthetic data indicated that if a westward electric field is present, as it happens often in the HR, the CR moves from the poleward boundary of the oval deep within the upward FAC region. This configuration prevents the standard current closure even for a balanced FAC and is well illustrated by our first event. More complicated FAC and conductance patterns, as in the second event, can also result in substantial FAC-EJ coupling, even if, again, the net FAC across the oval is zero. The two real data events, together with the synthetic data, suggest that the FAC-EJ

coupling might provide an important mechanism for the FAC closure in the HR, potentially relevant for all substorm phases. This is not surprising for the substorm WEJ [e.g., *Baumjohann*, 1983; *Fujii et al.*, 1994], but somewhat unexpected in other cases.

[68] The FAC-EJ coupling is consistent with azimuthal current closure in the magnetosphere. The magnetospheric part in the EEJ circuit enhances the ring current and contributes to its asymmetry, while in the WEJ circuit is opposite to the cross-tail current. The magnetospheric closure of the WEJ behaves as suggested by *Akasofu* [2003], and the sudden growth of the WEJ at the substorm onset results naturally in current disruption and dipolarization.

[69] Unlike in the model of *Akasofu* [2003], which relies on the standard Type 2 configuration suggested by *Boström* [1964], our configuration includes no meridional current loop. The magnetospheric generator is based on opposite electric field and current in dusk-dawn, instead of radial direction. In the ionosphere, the electrojet divergence appears to be controlled by the conductance, and in general dominated by the Hall component. Consequently, the Joule effect is small or missing, and the main load of the current circuit is located in the AAR. The energy is still dissipated in the ionosphere, but mostly by collisions of the accelerated particles.

[70] The work reported here will be continued by an extensive investigation of other HR events, in order to confirm the importance of the FAC-EJ coupling for the electrodynamics of this region. More work is needed also to confirm that the divergence of the electrojet is typically controlled by the conductance, in particular by the Hall conductance. The most interesting follow-up appears to be related to the auroral current circuit and to the substorm development. Considerable insight in this respect could be provided by the examination of Cluster and THEMIS data from the current disruption region, conjugate with low altitude and/or ground observations.

[71] **Acknowledgments.** O.M. acknowledges the warm hospitality of Max Planck Institute for Extraterrestrial Physics in Garching, as well as support in Romania through the CEEX project ALEGRO, contract 5942/2006, and the PECS project ECSTRA, contract C98048/2007.

[72] Wolfgang Baumjohann thanks the reviewers for their assistance in evaluating this paper.

References

Akasofu, S.-I. (1981), Energy coupling between the solar wind and the magnetosphere, *Space Sci. Rev.*, *28*, 121–190.

Akasofu, S.-I. (2003), A source of auroral electrons and the magnetospheric substorm current system, *J. Geophys. Res.*, *108*(A4), 8006, doi:10.1029/2002JA009547.

Akasofu, S.-I., and Y. Kamide (1998), Toward a closer integration of magnetospheric research: Magnetospheric currents inferred from ground-based magnetic data, *J. Geophys. Res.*, *103*, 14,939–14,958.

Baumjohann, W. (1983), Ionospheric and field-aligned current systems in the auroral zone: A concise review, *Adv. Space Res.*, *2*, 55–62.

Boström, R. (1964), A model of the auroral electrojets, *J. Geophys. Res.*, *69*, 4983–4999.

de la Beaujardière, O., R. Vondrak, and M. Baron (1977), Radar observations of electric fields and currents associated with auroral arcs, *J. Geophys. Res.*, *82*, 5051–5062.

Fontaine, D., and C. Peymirat (1996), Large-scale distributions of ionospheric horizontal and field-aligned currents inferred from EISCAT, *Ann. Geophys.*, *14*, 1284–1296.

Frey, H., W. Lieb, O. Bauer, H. Höfner, and G. Haerendel (1996), CCD-camera system for stereoscopic optical observations of the aurora, in *Current Developments in Optical Design and Engineering VI*, *SPIE Proc.*, vol. 2863, pp. 460–466, SPIE, Bellingham.

Fujii, R., R. Hoffman, P. Anderson, J. Craven, M. Sugiura, L. Frank, and N. Maynard (1994), Electrodynamic parameters in the nighttime sector during auroral substorms, *J. Geophys. Res.*, *99*, 6093–6112.

Galand, M., and A. Richmond (2001), Ionospheric electrical conductances produced by auroral proton precipitation, *J. Geophys. Res.*, *106*, 117–125.

Gjerloev, J., and R. Hoffman (2001), The convection electric field in auroral substorms, *J. Geophys. Res.*, *106*, 12,919–12,931.

Janhunen, P., A. Olsson, O. Amm, and K. Kauristie (2000), Characteristics of a stable arc based on FAST and MIRACLE observations, *Ann. Geophys.*, *18*, 152–160.

Kamide, Y., and S. Kokubun (1996), Two-component auroral electrojet: Importance for substorm studies, *J. Geophys. Res.*, *101*, 13,027–13,046.

Karlsson, T. (2001), Auroral electric fields from satellite observations and numerical modelling, Ph.D. thesis, Alfvén Laboratory, Royal Institute of Technology, Stockholm, Sweden.

Kauristie, K., M. Syrjäsuo, O. Amm, A. Viljanen, T. Pulkkinen, and H. Opgenoorth (2001), A statistical study of evening sector arcs and electrojets, *Adv. Space Res.*, *28*, 1605–1610.

Koskinen, H., and T. Pulkkinen (1995), Midnight velocity shear zone and the concept of Harang discontinuity, *J. Geophys. Res.*, *100*, 9539–9547.

Lyons, L., C.-P. Wang, and T. Nagai (2003), Substorm onset by plasma sheet divergence, *J. Geophys. Res.*, *108*(A12), 1427, doi:10.1029/2003JA010178.

Marghitu, O. (2003), Auroral arc electrodynamics with FAST satellite and optical data, Ph.D. thesis, Technische Universität Carolo-Wilhelmina, Braunschweig. (Available at http://www.biblio.tu-bs.de/ediss/data/20030606a/20030606a.html)

Marghitu, O., B. Klecker, G. Haerendel, and J. McFadden (2004), ALADYN: A method to investigate auroral arc electrodynamics from satellite data, *J. Geophys. Res.*, *109*, A11305, doi:10.1029/2004JA010474.

Nielsen, E., and R. Greenwald (1979), Electron flow and visual aurora at the Harang discontinuity, *J. Geophys. Res.*, *84*, 4189–4200.

Pfaff, R., C. Carlson, J. Watzin, D. Everett, and T. Gruner (2001), An overview of the Fast Auroral SnapshoT (FAST) satellite, *Space Sci. Rev.*, *98*, 1–32.

Robinson, R., R. Vondrak, K. Miller, T. Dabbs, and D. Hardy (1987), On calculating ionospheric conductances from the flux and energy of precipitating electrons, *J. Geophys. Res.*, *92*, 2565–2569.

Sugiura, M. (1984), A fundamental magnetosphere-ionosphere coupling mode involving field-aligned currents as deduced from DE-2 observations, *Geophys. Res. Lett.*, *11*, 877–880.

Weygand, J., R. McPherron, H. Frey, O. Amm, K. Kauristie, A. Viljanen, and A. Koistinen (2008), Relation of substorm onset to Harang discontinuity, *J. Geophys. Res.*, *113*(A4), A04213, doi:10.1029/2007JA012537.

G. Haerendel and B. Klecker, Max Planck Institute for Extraterrestrial Physics, Giessenbachstrasse, D-85748 Garching, Germany. (hae@mpe.mpg.de; berndt.klecker@ mpe.mpg.de)

T. Karlsson, Space and Plasma Physics, School of Electrical Engineering, Royal Institute of Technology, S-10044 Stockholm, Sweden. (tomas.karlsson@ee.kth.se)

O. Marghitu, Space Plasma and Magnetometry Group, Institute for Space Sciences, Atomistilor 409, P.O. Box MG-23, RO-77125 Bucharest, Romania. (marghitu@venus.nipne.ro)

J. McFadden, Space Sciences Laboratory, University of California, Berkeley, CA 94720-7450, USA. (mcfadden@ssl.berkeley.edu)